Multiscale topology optimization of electromagnetic metamaterials using a high-contrast homogenization method

Naoki Murai[a], Yuki Noguchi[a,b,*], Kei Matsushima[a], Takayuki Yamada[a,b]

[a] *Department of Mechanical Engineering, School of Engineering, The University of Tokyo, Yayoi 2-11-16, Bunkyo–ku, Tokyo 113-8656, Japan.*
[b] *Department of Strategic Studies, Institute of Engineering Innovation, School of Engineering, The University of Tokyo, Yayoi 2-11-16, Bunkyo–ku, Tokyo 113-8656, Japan.*

Abstract

This study proposes a multiscale topology optimization method for electromagnetic metamaterials using a level set-based topology optimization method that incorporates a high-contrast homogenization method. The high-contrast homogenization method can express wave propagation behavior in metamaterials for various frequencies. It can also capture unusual properties caused by local resonances, which cannot be estimated by conventional homogenization approaches. We formulated multiscale topology optimization problems where objective functions are defined by the macroscopic wave propagation behavior, and microstructures forming a metamaterial are set as design variables. Sensitivity analysis was conducted based on the concepts of shape and topological derivatives. As numerical examples, we offer optimized designs of metamaterials composed of multiple unit cell structures working as a demultiplexer based on negative permeability. The mechanism of the obtained metamaterials is discussed based on homogenized coefficients.

Keywords: Multiscale topology optimization, High-contrast homogenization method, Electromagnetic metamaterial, Level set method, Sensitivity analysis, Negative permiability

*Corresponding author. Tel.: +81-3-5841-0294; Fax: +81-3-5841-0294.
Email address: noguchi@mech.t.u-tokyo.ac.jp (Yuki Noguchi)

1. Introduction

Electromagnetic metamaterials are structural materials that exhibit electromagnetic properties not found in natural homogeneous materials. Both permeability and permittivity are material properties that describe the propagation characteristics of electromagnetic waves. Homogeneous materials in nature have different permittivity, and some metallic materials have a negative permittivity. However, most materials have a magnetic permeability of 1. The pioneering work by Pendry et al. [1] showed that negative permeability could be achieved by a metamaterial with a periodic array of split-ring resonators, which was experimentally verified by Smith et al. [2]. Later, Bouchitté and Felbacq [3] mathematically proved that for extensive material constant ratios in metamaterials, permeability exhibits a frequency response because of local resonance in the unit cell, with the real part of the permeability being negative near the resonance frequency. Furthermore, metamaterials that exhibit such negative permeability exhibit a bandgap that does not allow propagation of electromagnetic waves into the metamaterial in a certain frequency band, which may have applications such as filtering devices. Furthermore, metamaterials that exhibit negative permeability and permittivity exhibit a negative refractive index [4] and are expected to be used to realize innovative electromagnetic devices. Such devices are super lenses [5] that enable image formation beyond the diffraction limit, cloaking devices [6] that reduce scattered waves generated by obstacles, and compact antennas that can transmit THz waves [7].

Since metamaterials exhibit unique properties depending on their unit cell structure, the design of the unit cell is essential to realizing metamaterials with the desired electromagnetic properties. Conversely, it is difficult to design a unit cell structure by trial and error because metamaterials exhibit unique properties based on local resonance. Topology optimization is one solution to the problem. Topology optimization has the highest flexibility among structural optimization methods, leading to optimal design solutions based on mathematical models and optimization methods. There are many examples of structural problems, such as multimaterial structures [8] or structures with manufacturability [9] and other physical problems. Since Bendsøe and Kikuchi [10] proposed a method for structural problems, topology optimization has been developed for various physical fields such as heat conduction problems [11, 12] and wave problems such as sound waves [13] and electromagnetic waves [14]. It has also been applied to the design of electromag-

netic metamaterials that exhibit negative magnetic permeability [15, 16, 17].

In topology optimization, an objective function representing the performance and characteristics of the structure must be repeatedly evaluated, which requires iterative analysis of the target system. Since metamaterials are huge systems consisting of many unit cells with microstructures, metamaterial topology optimization requires introducing an appropriate estimating method. Smith et al. [18] proposed the S-parameter method to evaluate the macroscopic properties of metamaterials. This method replaces heterogeneous metamaterial structures with homogeneous materials with equivalent S-parameters and coefficients representing the complex reflectance and transmittance properties of the structure. This method can evaluate the negative properties of metamaterials. However, it assumes thin structures and plane incident waves, so the accuracy of evaluation can worsen depending on the designed metamaterial structure [19].

Another metamaterial estimating method is the homogenization method. This method replaces periodic structures with a homogeneous material that exhibits equivalent properties and is applied to structural problems [20, 21, 22]. In wave problems, the method was extended in several ways. The higher-order homogenization method [23, 24, 25] considers higher-order terms in the asymptotic expansion of the solution. However, it cannot treat the local resonance phenomena that cause unique properties of metamaterials. The high-frequency homogenization method [26] also takes an asymptotic expansion for the solution' s frequency. It can represent wave propagation behaviors even in local resonance phenomena but is effective only near the resonance frequency. A high-contrast homogenization method was recently proposed by Ohlberger and Verfürth [27] based on the settings in [3]. It is a method that introduces a scale to the material constants and can represent wave behaviors with high accuracy even in local resonance states. This method can be used in a wide range of frequency bands, unlike the high-frequency homogenization method.

This study proposes a multiscale topology optimization method for electromagnetic metamaterials with a high-contrast homogenization method. Structures of unit cells that contain metamaterials are optimized to minimize an objective function defined by wave propagation behavior on the macroscale. An optimization problem in which the design variable and objective function are defined on different scales is called a multiscale optimization problem. There are examples of optimal design of metamaterials using combined homogenization and multiscale topology optimization [28, 29]. Our

study aims to develop a method that enables the design of metamaterials operating at broadband frequencies consisting of multiple types of unit cell structures using high-contrast homogenization and multiscale optimization methods.

This paper is organized as follows. In Section 2, the electromagnetic metamaterial design problem is presented, and the high-contrast homogenization method is outlined. In Section 3, multiscale topology optimization problems are formulated, and a topology optimization method based on the level set method [30] is introduced. The design sensitivity is derived based on the concepts of shape and topological derivatives. In Section 4, the numerical implementation of the optimization method is described. In Section 5, the optimal design of a demultiplexer functioning at single and dual frequencies, as an example of an electromagnetic metamaterial, is presented in a two-dimensional numerical example. The resulting electromagnetic metamaterial with a periodically arranged unit cell structure is analyzed using the Helmholtz equation to demonstrate the validity of the designed unit cell structure.

2. High-contrast homogenization method for electromagnetic metamaterials

2.1. Outline of the metamaterial system

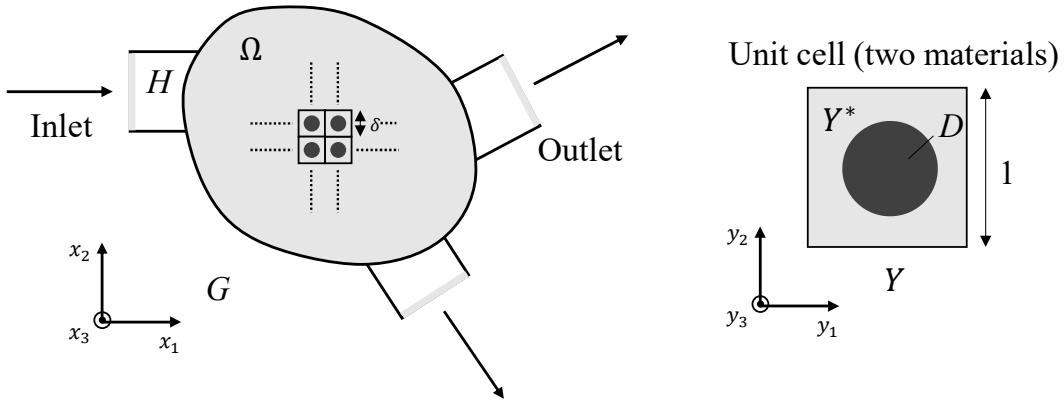

Figure 1: The sytem of an electromagnetic metamaterial.

This section explains the electromagnetic metamaterial system that will be optimized. As shown in Fig. 1, the system is composed of Region Ω, where square unit cells are arranged, and Region H is made of homogeneous material. Region G includes both regions. In Region Ω, the unit cells with size δ composed of two dielectric materials are arranged in a square lattice. We define the entire unit cell as Region Y and the region with an inclusion material as Region D, and $Y^* := Y \setminus D$. The inverse of the relative permittivity a_δ is defined in the regions as follows:

$$a_\delta(\boldsymbol{x}) = \begin{cases} \delta^2 \varepsilon_i^{-1} & \text{if } \boldsymbol{x} \in D, \\ \varepsilon_e^{-1} & \text{if } \boldsymbol{x} \in \Omega \setminus D, \\ 1 & \text{if } \boldsymbol{x} \in H. \end{cases} \tag{1}$$

Here, ε_i^{-1} is a complex number with positive real and imaginary parts defined with the square of the size of unit cells $\boldsymbol{\delta}$, and ε_e^{-1} is a positive real number. By this definition, if the unit cell δ approaches 0, the permittivity in Region D will be extremely larger than in Region Y^*. According to the literature [3], local resonances are evoked in unit cells when there is a large contrast between the permittivity of materials constituting the metamaterial, and it can exhibit a negative index. Assuming the harmonic oscillation of angular frequency ω, the transverse magnetic waves (called TM waves) enter the system with a component only in the x_3 direction magnetic field like $\boldsymbol{H} = (0, 0, u)^T$. The parameter u satisfies the Helmholtz equation defined in the $x_1 - x_2$ plane as follows:

$$-\nabla \cdot (a_\delta(\boldsymbol{x}) \nabla u) - k^2 u = 0 \qquad \text{in } \ G. \tag{2}$$

Here, k expresses the wave number and satisfies $k = \omega/c$, with the speed of light c. The first-order approximation of the Sommerfeld radiation condition is adopted to reduce reflected waves on the outer boundary of the analysis domain ∂G. The weak form of Eq. (2) is given as follows:

$$\int_G a_\delta(\boldsymbol{x}) \nabla u_\delta \cdot \nabla \psi - k^2 u_\delta \psi d\boldsymbol{x} = \int_{\partial G} g \psi d\Gamma \qquad \forall \psi \in H^1(G), \tag{3}$$

$$g = \begin{cases} iku_\delta \psi - 2iku_{\text{inc}} & \text{on } \ \Gamma_{\text{in}}, \\ iku_\delta \psi & \text{on } \ \Gamma_i, \\ 0 & \text{on } \ \Gamma_{\text{PEC}}. \end{cases} \tag{4}$$

In Eq. (3), the solution u is rewritten as u_δ because it depends on the size of the unit cells δ. Γ_{in} is the inlet, and Γ_i is the outlet of the system. The other boundary is made of a perfect electric conductor (denoted as PEC in the following).

2.2. High-contrast homogenization method

We introduce a high-contrast homogenization method proposed by previous work [27] to the system defined in Section 2.1. First, we introduce the microscale coordinate $\boldsymbol{y} = \boldsymbol{x}/\delta$ is to normalize the size of the unit cell and evaluate the two-scale convergence of u_δ in the extreme $\delta \to 0$. The two-scale convergence [31] expresses the convergence of function sequences where local resonances are evoked in microscale periodic structures.

According to the literature [27], the two-scale convergence of u_δ is expressed $u \in H^1(G)$, $u_1 \in L^2(\Omega; H^1_{\#,0}(Y^*))$, $u_2 \in L^2(\Omega; H^1_0(D)_\#)$ as:

$$u_\delta \xrightarrow{2} u(\boldsymbol{x}) + \chi_D(\boldsymbol{y})u_2(\boldsymbol{x}, \boldsymbol{y}), \tag{5}$$

$$\chi_{\Omega\setminus\bar{D}_\delta}\nabla u_\delta \xrightarrow{2} \chi_{Y^*}(\boldsymbol{y})(\nabla u(\boldsymbol{x}) + \nabla_y u_1(\boldsymbol{x}, \boldsymbol{y})), \tag{6}$$

$$\delta\chi_{D_\delta}\nabla u_\delta \xrightarrow{2} \chi_D(\boldsymbol{y})\nabla_y u_2(\boldsymbol{x}, \boldsymbol{y}), \tag{7}$$

$$\nabla u_\delta \xrightarrow{2} \nabla u \ \text{ in } G \setminus \bar{\Omega}. \tag{8}$$

$\xrightarrow{2}$ denotes two-scale convergence. χ is a characteristic function that takes 1 in the region shown by the subscript and takes 0 in the other regions. ∇_y represents the gradient in microscale $\boldsymbol{y}$. $H^1_{\#,0}(Y^*)$ and $H^1_0(D)_\#$ are subspaces of $H^1(Y^*)$ and $H^1(D)$, the Sobolev spaces satisfying periodic boundary conditions in unit cell Y, respectively. They are defined as follows:

$$H^1_{\#,0}(Y^*) := \{z \in H^1_\#(Y^*) | \int_{Y^*} z = 0\}, \tag{9}$$

$$H^1_0(D)_\# := \{z \in H^1_\#(D) | z = 0 \ \text{ on } \partial D\}. \tag{10}$$

The two-scale convergence written above is valid because Region Y^* is connected in the entire Region Ω [27]. The convergent sequences u, u_1, u_2 are the solutions of the weak form equation as follows:

$$B((u, u_1, u_2)(\psi, \psi_1, \psi_2)) = \int_{\partial G} g\psi^* d\Gamma, \quad \forall \boldsymbol{\psi} := (\psi, \psi_1, \psi_2)$$
$$\in H^1(G) \times L^2(\Omega; H^1_{\#,0}(Y^*) \times L^2(\Omega; H^1_0(D)_\#). \tag{11}$$

ψ, ψ_1 and ψ_2 represent test functions. B is defined with $\boldsymbol{u} := (u, u_1, u_2)$ as follows:

$$\begin{aligned} B(\boldsymbol{u}, \boldsymbol{\psi}) :=& \int_\Omega \int_{Y^*} \varepsilon_e^{-1} (\nabla u + \nabla_y u_1) \cdot (\nabla \psi^* + \nabla_y \psi_1^*) d\boldsymbol{y} d\boldsymbol{x} \\ &+ \int_\Omega \int_D \varepsilon_i^{-1} \nabla_y u_2 \cdot \nabla_y \psi_2^* d\boldsymbol{y} d\boldsymbol{x} \\ &- k^2 \int_G \int_Y (u + \chi_D u_2)(\psi^* + \chi_D \psi_2^*) d\boldsymbol{y} d\boldsymbol{x} \\ &+ \int_{G \setminus \bar{\Omega}} \nabla u \cdot \nabla \psi^* d\boldsymbol{x}. \end{aligned} \tag{12}$$

The homogenized equation is derived from the weak form Eq. (12) by solving u using relations $u_1(\boldsymbol{x}, \boldsymbol{y}) = \sum_{j=1}^2 \frac{\partial u}{\partial x_i}|_\Omega(\boldsymbol{x}) w_j(\boldsymbol{y})$, $u_2(\boldsymbol{x}, \boldsymbol{y}) = k^2 u|_\Omega(\boldsymbol{x}) w(\boldsymbol{y})$ as follows:

$$B_{\text{eff}}(u, \psi) = \int_{\partial G} g \psi d\Gamma \qquad \forall \psi \in H^1(G), \tag{13}$$

$$B_{\text{eff}}(u, \psi) := \int_G a_{\text{eff}} \nabla u \cdot \nabla \psi - k^2 \mu_{\text{eff}} u \psi d\boldsymbol{x}. \tag{14}$$

$a_{\text{eff}} \in \mathbb{R}^{2\times 2}$ and $\mu_{\text{eff}} \in \mathbb{C}$ are the homogenized coefficients that express the inverse of permittivity and the permeability, respectively. They are defined by the Kronecker delta δ_{jk} as follows:

$$(a_{\text{eff}}(\boldsymbol{x}))_{jk} = \begin{cases} \int_{Y^*} \varepsilon_e^{-1} (\boldsymbol{e}_j + \nabla_y w_j) \cdot (\boldsymbol{e}_k + \nabla_y w_k) d\boldsymbol{y} & \text{if } \boldsymbol{x} \in \Omega, \\ \delta_{jk} & \text{if } \boldsymbol{x} \in H, \end{cases} \tag{15}$$

$$\mu_{\text{eff}}(\boldsymbol{x}) = \begin{cases} \int_Y 1 + k^2 w \chi_D d\boldsymbol{y} & \text{if } \boldsymbol{x} \in \Omega, \\ 1 & \text{if } \boldsymbol{x} \in H. \end{cases} \tag{16}$$

w_j and w are the solutions of the Eq. (17) and (18) defined in the unit cells, respectively:

$$\int_{Y^*} \varepsilon_e^{-1} (\boldsymbol{e}_j + \nabla_y w_j) \cdot \nabla_y \psi_1 d\boldsymbol{y} = 0 \qquad \forall \psi_1 \in H^1_{\#,0}(Y^*), \tag{17}$$

$$\int_D \varepsilon_i^{-1} \nabla_y w \cdot \nabla_y \psi_2 - k^2 w \psi_2 d\boldsymbol{y} = \int_D \psi_2 d\boldsymbol{y} \qquad \forall \psi_2 \in H^1_0(D)_\#. \tag{18}$$

As written above, local resonances can be evoked in Region D at a frequency because the contrast of the material properties is significant [3]. The high-contrast homogenization method can approximate the original solution of Eq. (3) whether or not local resonances occur in Region D [27]. The

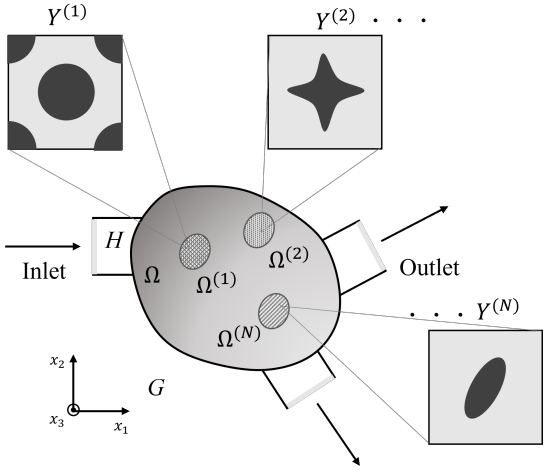

Figure 2: N unit cells of different structures $Y^{(i)}$ are arranged in each region $\Omega^{(i)}$ of metamaterial.

abovementioned homogenization procedure assumes that the metamaterial consists of the unit cells with the same structure. For metamaterials consisting of multiple unit cell structures, the homogenized coefficients should be treated as distributed in Ω. Let $\Omega^{(i)}$ $(i = 1, \cdots, N \quad \{N \in \mathbb{N} |\ N \geq 1\}) \in \Omega$ denote the N regions where unit cells of different structures are arrayed, and let $Y^{(i)}$ denote the unit cell of $\Omega^{(i)}$. The corresponding homogenized coefficients in $\Omega^{(i)}$ are given as follows:

$$(a_{\text{eff}}^{(i)}(\boldsymbol{x}))_{jk} = \begin{cases} \int_{Y^{*(i)}} \varepsilon_e^{-1}(\boldsymbol{e}_j + \nabla_y w_j^{(i)}) \cdot (\boldsymbol{e}_k + \nabla_y w_k^{(i)}) d\boldsymbol{y} & \text{if } \boldsymbol{x} \in \Omega^{(i)}, \\ \delta_{jk} & \text{if } \boldsymbol{x} \in H, \end{cases} \tag{19}$$

$$\mu_{\text{eff}}^{(i)}(\boldsymbol{x}) = \begin{cases} \int_{Y^{*(i)}} 1 + k^2 w^{(i)} \chi_D d\boldsymbol{y} & \text{if } \boldsymbol{x} \in \Omega^{(i)}, \\ 1 & \text{if } \boldsymbol{x} \in H. \end{cases} \tag{20}$$

$w_j^{(i)}$ and $w^{(i)}$ are the solutions of the following equations rewritten from

Eqs. (17) and (18):

$$\int_{Y^{*i}} \varepsilon_e^{-1}(\boldsymbol{e}_j + \nabla_y w_j^{(i)}) \cdot \nabla_y \psi_1^{(i)} d\boldsymbol{y} = 0$$
$$\forall \psi_1^{(i)} \in H^1_{\#,0}(Y^{*i}), \tag{21}$$
$$\int_{D^{(i)}} \varepsilon_i^{-1} \nabla_y w^{(i)} \cdot \nabla_y \psi_2^{(i)} - k^2 w^{(i)} \psi_2^{(i)} d\boldsymbol{y} = \int_{D^{(i)}} \psi_2^{(i)} d\boldsymbol{y}$$
$$\forall \psi_2^{(i)} \in H^1_0(D^{(i)})_{\#}. \tag{22}$$

Using the spatially distributed homogenized coefficients, the homogenized Eq. (14) can be rewritten as follows:

$$B_{\text{eff}}(u, \psi) = \sum_{i=1}^{N} \left[\int_G a_{\text{eff}}^{(i)}(\boldsymbol{x}) \nabla u \cdot \nabla \psi - k^2 \mu_{\text{eff}}^{(i)}(\boldsymbol{x}) u \psi d\boldsymbol{x} \right]. \tag{23}$$

By setting unit cells of different structures, it is possible to optimize metamaterials of diverse structures that perform better than unit cells of the same structure.

3. Topology optimization

3.1. Formulation of a multiscale topology optimization problem

Here, we explain a multiscale topology optimization method for metamaterials. This method minimizes objective functions defined with macroscopic wave propagation behaviors by optimizing microscale structures. In this paper, we design a demultiplexer that guides incident waves to an outlet corresponding to frequency, as shown in Fig. 3. It has one inlet Γ_{in} and two outlets (Γ_1 and Γ_2). $N = 16$ different unit cells arrayed in Ω. The design variables are the unit cell configurations in Regions $\Omega^{(i)}$ ($i = 1, \cdots, N$). Each Region $\Omega^{(i)}$ is a square of the same size.

Two numerical examples are presented in Section 5. One is a metamaterial operating at a single wavenumber $k = k_1$, and the other is a metamaterial operating at two different wavenumbers $k = k_1$ and $k = k2$. The objective functions of the metamaterials acting as a demultiplexer are defined as fol-

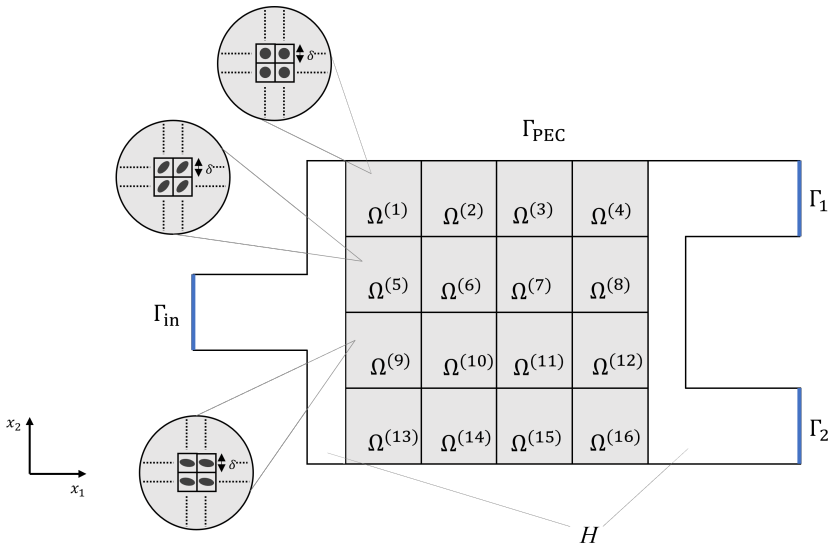

Figure 3: The setting of metamaterial in the optimization problem.

lows:

$$J_1 = J_{k1}, \tag{24}$$

$$J_2 = J_{k1} + J_{k2}, \tag{25}$$

$$J_{k1} = \left.\frac{\int_{\Gamma_1} |u|^2 d\Gamma}{\int_{\Gamma_2} |u|^2 d\Gamma}\right|_{k=k_1}, \tag{26}$$

$$J_{k2} = \left.\frac{\int_{\Gamma_2} |u|^2 d\Gamma}{\int_{\Gamma_1} |u|^2 d\Gamma}\right|_{k=k_2}. \tag{27}$$

J_{k1} and J_{k2} express the ratio of the square of the wave amplitude on two outlets, Γ_1 and Γ_2. By minimizing the objective function J_1, the incident wave from the inlet Γ_{in} almost travels through the outlet Γ_2 at k_1. Minimizing J_2 corresponds to designing a metamaterial that acts as a demultiplexer switching between k_1 and k_2. In an optimal metamaterial, the amplitude on Γ_2 is larger than that on Γ_1 at k_1. Contrarily, the amplitude on Γ_1 is larger than that on Γ_2 at k_2.

From the above, the optimization problem is formulated as follows:

$$\begin{aligned}
&\min_{Y^{(1)},\cdots,Y^{(N)}} \quad J_1 \text{ or } J_2 \quad ((24),(25)) \\
&\text{subject to} \quad \text{Governing equations in } Y^{(i)} \ (i=1,\cdots,N) \quad ((21),(22)), \\
&\qquad\qquad \text{Governing equations in } G \quad ((23)), \\
&\qquad\qquad \text{Expressions of } (a_{\text{eff}}^{(i)}, \mu_{\text{eff}}^{(i)}) \ (i=1,\cdots,N) \quad ((19),(20)).
\end{aligned} \tag{28}$$

3.2. Level set-based topology optimization

To solve the optimization problem (28), we use the topology optimization based on a level set method proposed by Yamada et al. [30]. In this method, the configuration of N unit cells in each design domain $\Omega^{(i)}$ is expressed by an isosurface of level set functions $\phi^{(i)}$ corresponding to $Y^{(i)}$. $\phi^{(i)}$ is defined as follows:

$$\begin{cases}
0 < \phi^{(i)}(\boldsymbol{y}) \leq 1 & \text{if } \boldsymbol{y} \in \ Y^{*(i)} \backslash \partial Y^{*(i)}, \\
\phi^{(i)}(\boldsymbol{y}) = 0 & \text{if } \boldsymbol{y} \in \ \partial Y^{*(i)}, \\
-1 \leq \phi^{(i)}(\boldsymbol{y}) < 0 & \text{if } \boldsymbol{y} \in \ D^{(i)} \backslash \partial Y^{*(i)}.
\end{cases}$$

The region satisfying $\phi^{(i)} > 0$ is $Y^{*(i)}$, the region satisfying $\phi^{(i)} < 0$ is $D^{(i)}$, and the boundary satisfying $\phi^{(i)} = 0$ is $\partial Y^{*(i)}$. Since unit cells are arranged periodically, a periodic boundary condition is applied to $\phi^{(i)}$. Using this expression, the optimization problem (28) is rewritten as follows:

$$\begin{aligned}
&\min_{\phi^{(1)}(\boldsymbol{y}),\cdots,\phi^{(N)}(\boldsymbol{y})} \quad J_1 \text{ or } J_2 \\
&\text{subject to} \quad \text{Governing equations in } Y^{(i)} \ (i=1,\cdots,N), \\
&\qquad\qquad \text{Governing equations in } G, \\
&\qquad\qquad \text{Expressions of } (a_{\text{eff}}^{(i)}, \mu_{\text{eff}}^{(i)}) \ (i=1,\cdots,N).
\end{aligned} \tag{29}$$

To solve the optimization problem (29), a fictitious time t is introduced, and $\phi^{(i)}$ is updated using the design sensitivity of the objective function. The level set function $\phi^{(i)}$ is updated by the following reaction–diffusion equation.

$$\frac{\partial \phi^{(i)}}{\partial t} = -K(J'^{(i)} - \tau \nabla_y^2 \phi^{(i)}) \qquad \text{in } Y^{(i)}, \tag{30}$$

$K(>0)$ is a constant, and J' is the design sensitivity defined with topological and shape derivatives; the details of which are given in Section 3.3. τ is an

appropriate small positive number defined as a regularization parameter and is used to regularize the optimization problem. The optimal level set function $\phi^{(i)}$ can be found by solving the reaction–diffusion equation (30) with periodic boundary conditions on the outer boundary of Region $Y^{(i)}$.

3.3. Sensitivity analysis

We derive the shape derivative and the topological derivative used as the design sensitivity for the optimization problem.

The shape derivative is the variation rate of the objective function when Region D_0 is transformed into Region $D' = \{\boldsymbol{x} + t\boldsymbol{\theta}(\boldsymbol{x}) \mid \boldsymbol{x} \in D_0\}$ based on the vector field $\boldsymbol{\theta}(\boldsymbol{x})$ (Fig. 4(a)) and is defined as follows:

$$DJ(D_0) \cdot \boldsymbol{\theta} = \lim_{t \to 0} \frac{J(D') - J(D_0)}{t}. \tag{31}$$

The topological derivative is the variation rate of the objective function J when an infinitesimal circular inclusion Region D_ε of radius ε is placed in Region Y^* (Fig. 4(b)) and is defined as follows:

$$D_T J = \lim_{\varepsilon \to 0} \frac{J(Y^* \setminus \overline{D}_\varepsilon) - J(Y^*)}{V(\varepsilon)}. \tag{32}$$

$V(\varepsilon)$ is determined such that the right side of the equation (32) exist. In this research, we use $V(\varepsilon) = -\pi\varepsilon^2$. There are two reasons to use them simulta-

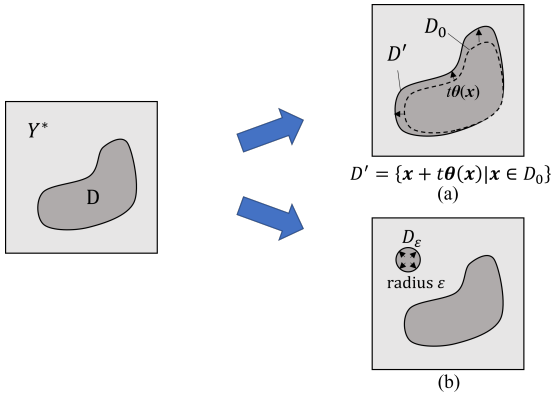

Figure 4: Assumed configuration changes in design sensitivity: (a) shape change assumed in the shape derivative and (b) topological change assumed in the topological derivative.

neously. First, the topological derivative assumes that the point is not close to the boundaries. The shape derivative is more appropriate to the sensitivity of the boundaries. Second, we should optimize unit cell configurations so that $Y^{*(i)}$ is connected since that is the restriction for the high-contrast homogenization method to hold. The topological derivative in $D^{(i)}$ can break this constraint, so we used the shape derivative on $\partial D^{(i)}$ instead. The validity of introducing topological and shape derivatives into the level set-based topology optimization method [30] has been demonstrated previously [32]. The design sensitivity is presented as follows using the shape (34)–(39) and topological derivatives (42):

$$J'^{(i)}(\boldsymbol{y}) = g(DJ(Y^{*(i)}) \cdot \boldsymbol{\theta}, DJ(D^{(i)}) \cdot \boldsymbol{\theta}, D_T J^{(i)})(\boldsymbol{y}) \tag{33}$$

We derive the shape derivatives using Céa's method [33]. The derivatives are derived as follows:

$$DJ(Y^{*(i)}) \cdot \boldsymbol{\theta} = \int_{\partial Y^{*(i)}} (\boldsymbol{\theta} \cdot \boldsymbol{n}) j_1^{(i)} d\Gamma, \tag{34}$$

$$j_1^{(i)} = 2\mathrm{Re}\left[\lambda_{a_{jk}}^{(i)}\right] \varepsilon_e^{-1}(\delta_{jk} + \frac{\partial w_j^{(i)}}{\partial y_k} + \frac{\partial w_k^{(i)}}{\partial y_j} + \nabla_y w_j^{(i)} \cdot \nabla_y w_k^{(i)}), \tag{35}$$

$$\lambda_{a_{jk}}^{(i)} = \int_{\Omega^{(i)}} \frac{\partial u}{\partial x_k} \frac{\partial v_l}{\partial x_j} d\boldsymbol{x}, \tag{36}$$

$$DJ(D^{(i)}) \cdot \boldsymbol{\theta} = \int_{\partial D^{(i)}} (\boldsymbol{\theta} \cdot \boldsymbol{n}) j_2^{(i)} d\Gamma \tag{37}$$

$$j_2^{(i)} = 2\mathrm{Re}\left[\lambda_\mu^{(i)}\right] \mathrm{Re}\left[2k^2\left\{\boldsymbol{n} \cdot (\varepsilon_i^{-1} \nabla_y w^{(i)})(\boldsymbol{n} \cdot \nabla_y w^{(i)})\right\} - k^2 \varepsilon_i^{-1} \nabla_y w^{(i)} \cdot \nabla_y w^{(i)}\right], \tag{38}$$

$$\lambda_\mu^{(i)} = -\int_{\Omega^{(i)}} k^2 u v_l d\boldsymbol{x}. \tag{39}$$

v_l is an adjoint variable and substituted by v_1 or v_2 corresponding to the objective function J_{k1} or J_{k2}. The adjoint equations corresponding to v_1 and

v_2 are defined as follows:

$$\sum_{i=1}^{N}\left[\int_{\Omega^{(i)}} a_{\text{eff}}^{(i)}\nabla v_1\cdot\nabla\psi - k^2\mu_{\text{eff}}^{(i)}v_1\psi d\boldsymbol{y}\right] - ik\int_{\Gamma_{\text{in}},\Gamma_1,\Gamma_2} v_1\psi d\Gamma$$
$$+\frac{1}{W_2}\int_{\Gamma_1} u^*\psi d\Gamma - \frac{W_1}{W_2^2}\int_{\Gamma_2} u^*\psi d\Gamma = 0, \tag{40}$$
$$\sum_{i=1}^{N}\left[\int_{\Omega^{(i)}} a_{\text{eff}}^{(i)}\nabla v_2\cdot\nabla\psi - k^2\mu_{\text{eff}}^{(i)}v_2\psi d\boldsymbol{y}\right] - ik\int_{\Gamma_{\text{in}},\Gamma_1,\Gamma_2} v_2\psi d\Gamma$$
$$-\frac{W_2}{W_1^2}\int_{\Gamma_1} u^*\psi d\Gamma + \frac{1}{W_1}\int_{\Gamma_2} u^*\psi d\Gamma = 0. \tag{41}$$

Here $W_1 = \int_{\Gamma_1}|u|^2 d\Gamma, W_2 = \int_{\Gamma_2}|u|^2 d\Gamma$, and u^* is complex conjugate of u.

Then, we derive the topological derivatives from the shape derivatives (34)–(39). Using the method proposed by Novotny et al. [34] and Feijó et al. [35], which derives the topological derivative from the limit of the shape derivative, the topological derivatives can be derived as follows:

$$D_T J^{(i)} = 2\text{Re}\left[\lambda_{a_{jk}}^{(i)}\right]\varepsilon_e^{-1}\{\delta_{jk} + \boldsymbol{e}_j\cdot\nabla_y w_k^{(i)} + \boldsymbol{e}_k\cdot\nabla_y w_j^{(i)}$$
$$+2\nabla_y w_j^{(i)}\cdot\nabla_y w_k^{(i)} + \delta_{kl}\frac{\partial w_j^{(i)}}{\partial y_l} + \delta_{jl}\frac{\partial w_k^{(i)}}{\partial y_l} + \delta_{jl}\delta_{kl}\}. \tag{42}$$

The details of the derivation process for the shape and topological derivatives are given in Appendix A.

4. Numerical implementation

The optimization procedure is based on the algorithm as below.
***step* 1**: Define initial configuration and parameters
***step* 2**: Solve Eqs. (21) and (22) in N unit cells $Y^{(i)}$ $(i = 1, \cdots, N)$ by the finite element method (FEM)
***step* 3**: Compute the homogenized coefficients (19) and (20) corresponding to each $\Omega^{(i)}$ $(i = 1, \cdots, N)$
***step* 4**: Solve the homogenized equation (23) by FEM
***step* 5**: Compute the objective function (24) or (25)
***step* 6**: If the objective function converges, the optimization is terminated; otherwise, proceed to ***step* 7**

***step* 7**: Solve the adjoint equation (40) by FEM
***step* 8**: Compute the sensitivities (34)–(39) and (42) in each unit cell $Y^{(i)}$ $(i = 1, \cdots, N)$
***step* 9**: Update the level set functions $\phi^{(i)}$ $(i = 1, \cdots, N)$ corresponding to configuration of N unit cells $Y^{(i)}$ by reaction-diffusion equation (43)
***step* 10**: Remesh N unit cells $Y^{(i)}$ $(i = 1, \cdots, N)$ based on the updated level set functions
***step* 11**: Back to ***step* 2**

If the objective function is J_2, the processes in ***steps* 2**, **3**, **4**, **7**, and **8** should be performed. The way to treat the sensitivities computed in ***step* 8** for each wavenumber is explained in Section 4.2. First, the governing and adjoint equations are solved by an open-source FEM solver FreeFem++ [36]. Then, in***step* 9**, a remeshing procedure is introduced so that the boundary of the finite element and the boundary of the inclusion domain $\partial D^{(i)}$ coincide. This is necessary to impose Dirichlet boundary conditions on $\partial D^{(i)}$ in Eq. (22). Additionally, reducing numerical errors that can occur because of boundary mismatch is useful. To do so, the open-source remesher, Mmg [37], was used.

The reaction diffusion equation (30) is discretized as follows:

$$\phi^{(i)} - \phi^{(i)}_{\mathrm{pre}} = -K(J'^{(i)} - \tau \nabla_y^2 \phi^{(i)})\Delta t. \tag{43}$$

$\phi^{(i)}_{\mathrm{pre}}$ is the previous level set function, and Δt is the width of fictitious time step.

4.1. Extension of shape derivatives

To stabilize the optimization, the shape derivatives derived in Section 3 were extended to the entire Region Y by solving an equation proposed in the literature [38]:

$$\int_{Y^{(i)}} (\alpha^2 \nabla_y Q_l^{(i)} \cdot \nabla_y \psi + Q_l^{(i)} \psi) d\boldsymbol{y} = \int_{\partial D^{(i)}} j_l \psi d\Gamma. \tag{44}$$

Here, j_l $(l = 1, 2)$ is the sensitivity defined by (35) and (38), and α is a positive parameter that expresses the magnitude of extension. Q_l is the sensitivity extended from j_l. In Section 5, we used $\alpha^2 = 0.05$. According to the method in the previous study [11], the calculation of boundary integral

on the right-hand side of Eq. (44) is approximated with $\delta_{\partial D^{(i)}}(\boldsymbol{y})$ defined by the level set function as follows:

$$\int_{\partial D^{(i)}} j_l \psi d\Gamma \approx \int_{Y^{(i)}} \delta_{\partial D^{(i)}}(\boldsymbol{y}) j_l \psi d\boldsymbol{y}, \tag{45}$$

where $\delta_{\partial D^{(i)}}(\boldsymbol{y})$ denotes the approximated delta function, defined as follows:

$$\delta_{\partial D^{(i)}}(\boldsymbol{y}) = \frac{1}{2}|\nabla_y Se^{(i)}|, \tag{46}$$

$$Se^{(i)} = \frac{\phi^{(i)}}{\sqrt{\phi^{i2} + \epsilon_\delta^2}}. \tag{47}$$

where ϵ_δ is a parameter indicating the transition width of the approximated delta function. In the numerical example, we set $\epsilon_\delta = 0.1$. Then, using the extended sensitivity on the right-hand side of the reaction − diffusion equation (30), the optimization becomes stable.

4.2. Definition of design sensitivity

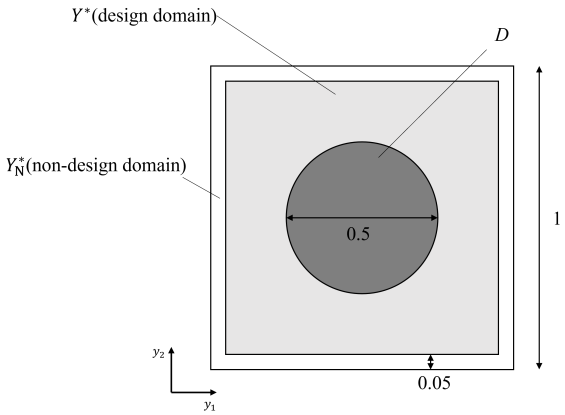

Figure 5: The setting and initial configuration of unit cell. Y_{N}^* is made of matrix material and non-design domain.

The two-scale convergence in the high-contrast homogenization method assumes that the matrix region is all connected, as mentioned in Section 2. Hence, configurations should be updated without breaking the connectivity in the optimization. As shown in Fig. 5, a nondesign domain Y_{N}^* with a width of 0.05 (y-coordinate) consisting of matrix material was set outside

the square unit cells. The design sensitivity $J'^{(i)}$ was set to 0 in Region D to restrict the unconnected configuration. In optimization, updates to the level set functions corresponding to the generation of $Y^{(i)}$ in the inclusion domain $D^{(i)}$ must be restricted because they break the connectivity. Thus, we ignored the design sensitivity within $D^{(i)}$. To do so, we defined a region where the design sensitivity is ignored by an approximate Heaviside function:

$$H(\phi) = \begin{cases} 1 & (|\phi| > \phi_{low} + \epsilon), \\ \frac{1}{2} - \frac{|\phi| - \phi_{low}}{2\epsilon} - \frac{1}{2\pi}\sin\left[\frac{\pi(|\phi| - \phi_{low})}{\epsilon}\right] & (\phi_{low} - \epsilon \leq |\phi| \leq \phi_{low} + \epsilon), \\ 0 & (|\phi| < \phi_{low} - \epsilon). \end{cases} \tag{48}$$

ϵ is a parameter that indicates the variation width and is set as $\epsilon = 0.01$. $H(\phi)$ equals 1 in the Regions Y_{N}^*, Y^*, and D, except for the boundary ∂D and 0 on the boundary ∂D. After all, the sensitivity $J'^{(i)}$ used on the right-hand side of the reaction − diffusion equation is defined as follows:

$$\begin{aligned} J'^{(i)} &= g(DJ(Y^{*(i)}) \cdot \boldsymbol{\theta}, DJ(D^{(i)}) \cdot \boldsymbol{\theta}, D_T J^{(i)})(\boldsymbol{y}) \\ &\quad \frac{D_T J^{(i)}}{AbsD_T J} \chi_{Y^*} H(\phi^{(i)}) + \left(\frac{Q_1^{(i)}}{AbsQ_1} - \frac{Q_2^{(i)}}{AbsQ_2} \right) (1 - H(\phi^{(i)})), \end{aligned} \tag{49}$$

$$AbsD_T J = \frac{1}{N} \sum_{i=1}^{N} \frac{\int_{Y^{*(i)}} D_T J^{(i)} d\boldsymbol{y}}{\int_{Y^{*(i)}} d\boldsymbol{y}},$$

$$AbsQ_1 = \frac{1}{N} \sum_{i=1}^{N} \frac{\int_{Y^{(i)}} Q_1^{(i)} (1 - H(\phi^{(i)})) d\boldsymbol{y}}{\int_{Y^{(i)}} (1 - H(\phi^{(i)})) d\boldsymbol{y}}, \quad AbsQ_2 = \frac{1}{N} \sum_{i=1}^{N} \frac{\int_{Y^{(i)}} Q_2^{(i)} (1 - H(\phi^{(i)})) d\boldsymbol{y}}{\int_{Y^{(i)}} (1 - H(\phi^{(i)})) d\boldsymbol{y}}.$$

$Q_1^{(i)}$ and $Q_2^{(i)}$ are calculated by Eq. (44), substituting $j_1^{(i)}, j_2^{(i)}$, respectively. $AbsD_T J$, $AbsQ_1$ and $AbsQ_2$ are used for the normalization.

In the optimization of $J = J_2$, the sensitivities of J_{k1} and J_{k2} are calculated respectively, and their sum is substituted in $J'^{(i)}$.

5. Numerical examples

In this section, the effectivity of the proposed optimization method is demonstrated with numerical examples. We offer two optimization examples for metamaterials that work as demultiplexers. In Section 5.1, the objective

function J_1 is minimized for a single-frequency input wave. In Section 5.3, we minimized J_2 to obtain the optimized design of a metamaterial operating at two frequencies. Fig. 6 shows the setting of the computational domain. Γ_{in} is the inlet, and Γ_1 and Γ_2 are the outlets. The white regions are H consisting of homogeneous material, and the gray region is the design domain Ω divided into 16 regions $\Omega^{(i)}$. Additionally, the optimal configuration in Section 5.1 obtained by the proposed method based on the high-contrast homogenization method is verified by solving the Helmholtz equation (3) for the metamaterial composed of finite numbers of a periodic array of optimized unit cells.

The inverse permittivities and the wavenumbers are given as $\varepsilon_e^{-1} = 10[\text{m/F}]$, $\varepsilon_i^{-1} = 10 - 0.01i[\text{m/F}]$, $k_1 = 28$ and $k_2 = 38$. The regularization parameter in Eq. (43) is given as $\tau = 1.0 \times 10^{-4}$, and the width of fictitious time step Δt in Eq. (43) is given depending on the value of the objective functions. In Section 5.1, $\Delta t = 1.0 \times 10^{-3}$ if $J_1 \leq 0.3$, or $\Delta t = 5.0 \times 10^{-3}$. In Section 5.3, $\Delta t = 1.0 \times 10^{-3}$ if $J_{k1} \leq 0.5$ and $J_{k2} \leq 0.5$, or $\Delta t = 5.0 \times 10^{-3}$. The incident wave is given as a plane wave $u_{\text{inc}} = \exp(ikx_1)$.

5.1. Single-frequency optimization

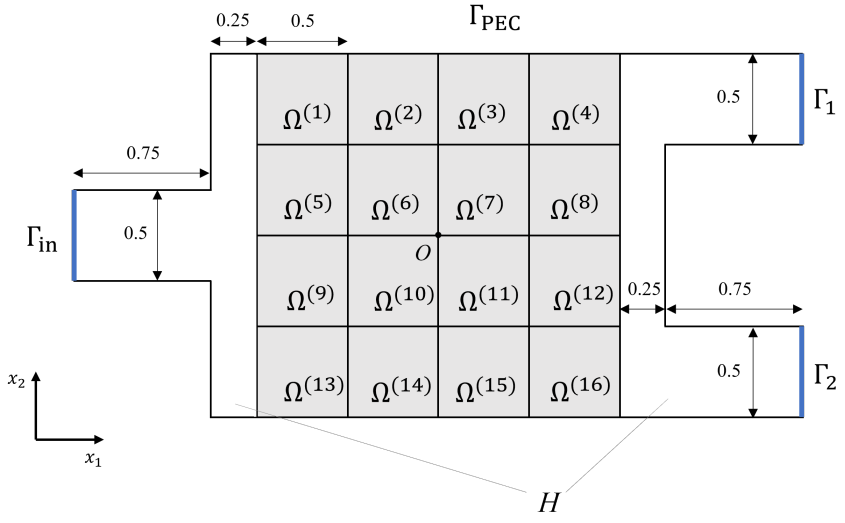

Figure 6: The setting of the computational domain. The units are in [m].

Here, we demonstrate that our optimization method is valid for designing metamaterials. The initial configuration of each unit cell is the same as shown

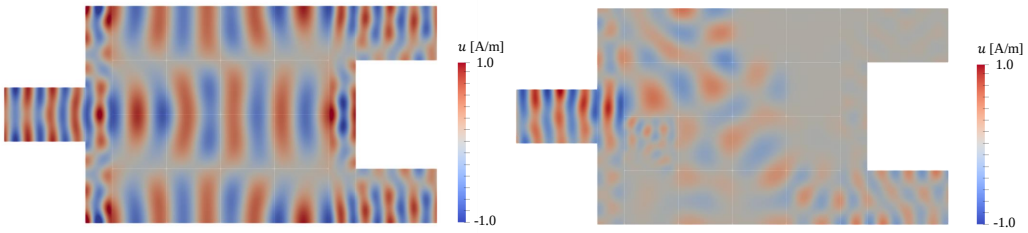

(a) (b)

Figure 7: Distribution of real part of u at $k = k_1$; (a): the intial configuration (b): optimal configurations.

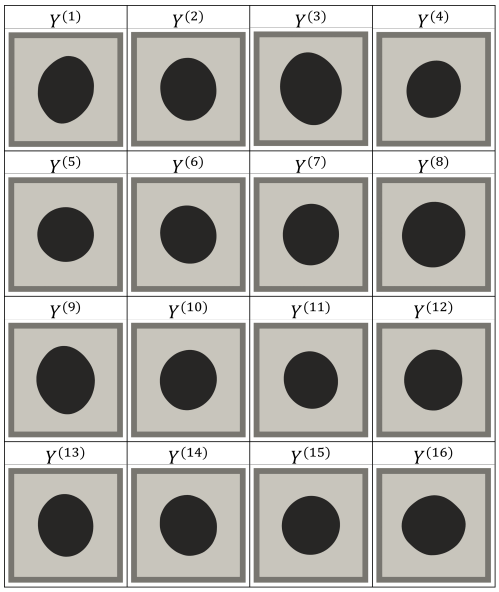

Figure 8: The optimal configrations of unit cells $Y^{(i)}$ obtained in single-frequency optimization

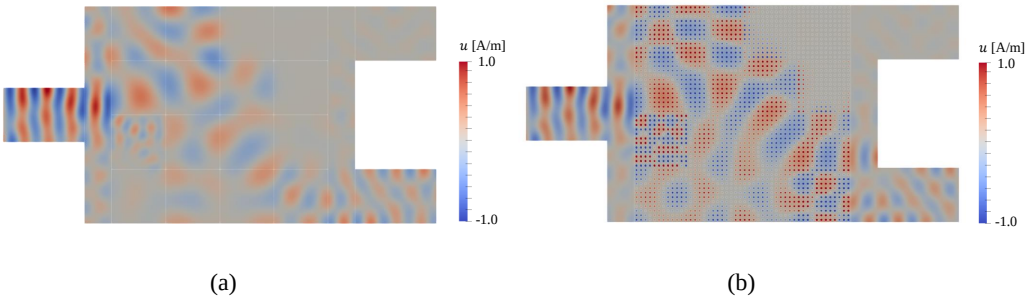

(a) (b)

Figure 9: (a): Distribution of real part of u obtained with the homogenized equation and the optimal configurations; (b): the solution of Helmholtz equation in the arrayed optim unit cells.

in, where the circular inclusion Region $D^{(i)}$ of radius 0.25 is placed in the center. The homogenized coefficients of the initial configuration are $a_{11} = 6.65$, $a_{12} = -3.49 \times 10^{-5}$, $a_{21} = 2.62 \times 10^{-3}$, $a_{11} = 6.65$, and $\mu = 1.76 + 0.00490i$, and Fig. 7(a) shows the wave propagation behavior Re(u). The objective function is J_1 (Eq. (24)), and the value is 1.00 with the initial configuration consistent with the symmetry of the geometry and the boundary condition.

As a result of optimization, we obtained the optimal configuration, as shown in Fig. 8. Compared with the initial configuration, the radius and aspect ratio of Region $D^{(i)}$ were changed. The value of the objective function is 0.0163, and Fig. 7(b) shows the wave propagation in the optimized system. Fig. 10 shows the homogenized coefficients of the optimal configuration. $a_{11}^{(i)}$ and $a_{22}^{(i)}$ did not change significantly. The range of the values is $5.52 \leq a_{11}^{(i)} \leq 6.94$ and $6.12 \leq a_{22}^{(i)} \leq 6.95$. Conversely, the range of $a_{12}^{(i)}$ and $a_{21}^{(i)}$ are $-0.120 \leq a_{12}^{(i)} \leq 0.138$ and $-0.120 \leq a_{21}^{(i)} \leq 0.138$, that is larger than the initial configuration but the effect of the values is small. Re $\left[\mu^{(i)}\right]$ is in the range $1.5 \leq \text{Re}\left[\mu^{(i)}\right] \leq 3.0$ in most regions. However, there are some regions local resonance occurs, where absolute value of Re $\left[\mu^{(i)}\right]$ may be large, or the sign may differ from the relative permeability of the materials that make up the unit cell. In $\Omega^{(9)}$, μ shows large value: Re $\left[\mu^{(9)}\right] = 14.0$. And as an remarkable point, μ has negative real part in $\Omega^{(3)}$ and $\Omega^{(8)}$: Re $\left[\mu^{(3)}\right] = -0.832$, Re $\left[\mu^{(8)}\right] = -2.16$, respectively.

One of the factors contributing to the decrease in the objective function is the bandgap region. The propagation of waves corresponding to the wavenumber $k = k_1$ is forbidden in regions where $\mu^{(i)}$ calculated by the

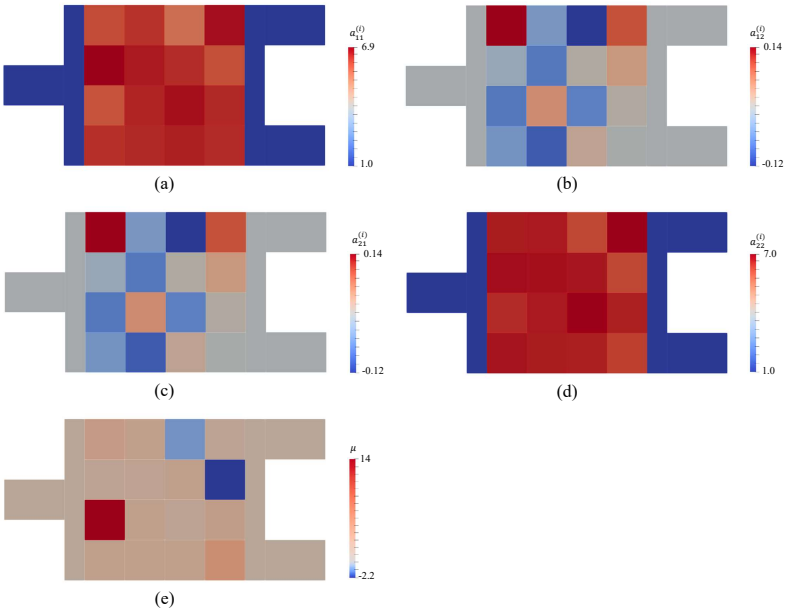

Figure 10: Distribution of the homogenized coefficients. (a): $a_{11}^{(i)}$; (b): $a_{12}^{(i)}$; (c): $a_{21}^{(i)}$; (d): $a_{22}^{(i)}$; (e): Re $\left[\mu^{(i)}\right]$.

high-contrast homogenization method is negative [27]. Fig. 9 shows little wave transmission in $\Omega^{(3)}$ and $\Omega^{(8)}$. The bandgap prevents the wave from propagating to Γ_1.

The contrast between Re $\left[\mu^{(12)}\right]$ and Re $\left[\mu^{(16)}\right]$ is also a factor as it causes wave impedance in $\Omega^{(16)}$ larger than that in $\Omega^{(12)}$, guiding the wave in the direction of Γ_2. The wave impedance is given by the bandgap in $\Omega^{(3)}$ and $\Omega^{(8)}$ cannot block the wave traveling to Γ_1 through $\Omega^{(12)}$ and $\Omega^{(16)}$. Hence, the second factor is also important to the optimization results.

5.2. The verification for the optimal configurations

Here, we compare the wave propagation behavior obtained by the homogenized equation (23) with the solution obtained by the Helmholtz equation in Eq. (2) in a 12×12 system with an array of optimized unit cells in each region. The size of the unit cell is set to $\delta = 1/24$. Fig. 9(b) presents the solution of the Helmholtz equation. The performance guiding the wave to the border of Γ_2 is observed in both solutions as the most important point. Fig. 11 shows the frequency response of the objective function J_1 calculated

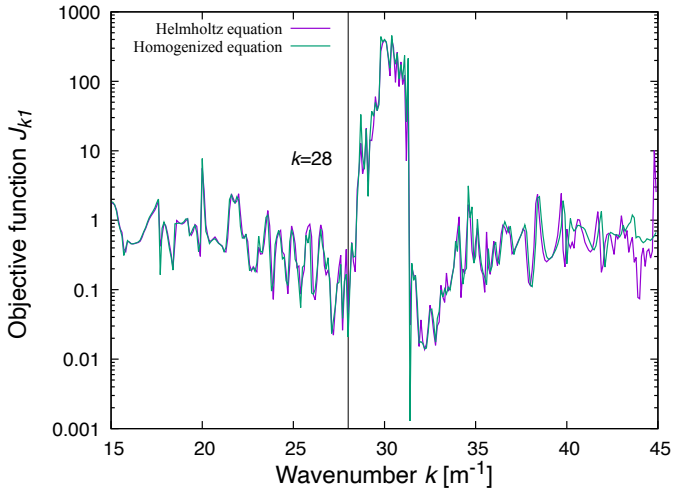

Figure 11: Frequency response of the object function J_{k1} calculated with the solutions of the homogenized equation and Helmholtz equation.

from the solutions of the homogenized equation (23) and the Helmholtz equation in Eq. (2). Both have a peak at the target frequency $k = 28$, and the responses are similar overall. The value of the object function (24) calculated from the solution of the homogenized equation (Fig. 9(a)) is 0.0163, and that calculated through verification (Fig. 9(b)) is 0.0461. The two values of the objective function do not match exactly, and there is a gap between them. There are some possible reasons for this. First, the numerical analysis of the Helmholtz equation does not meet the homogenization assumption that the unit cells are almost zero in size, and the unit cells are arranged in an infinite array. Second, the region unit cells are arranged touching other regions or PEC walls. This situation is not considered in the homogenization method. The second reason cannot be solved in the setting of the optimization problem, but the first reason can be improved by reducing δ. Despite some problems, the differences are quite small to demonstrate the validity of estimating the performance of metamaterials with the high-contrast homogenization method. The optimized metamaterial behaved as intended, indicating the effectiveness of the optimization method.

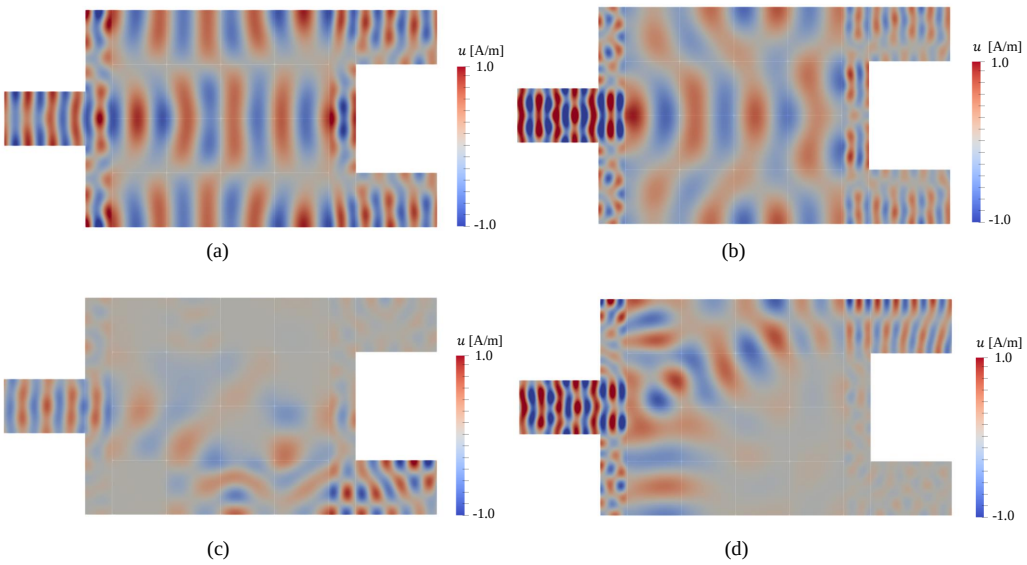

Figure 12: Distribution of real part of u. (a): with initial configurations, $k = k_1$; (b): with initial configurations, $k = k_2$; (c): with optimal configurations, $k = k_1$; (d): with optimal configurations, $k = k_2$.

5.3. Two-frequency optimization

We present the optimal configuration of the metamaterial operating at two frequencies here. The initial configuration is the same as in Section 5.1. The homogenized coefficient μ depends on wavenumber: $\mu = 0.635+0.000694i$ at $k = k_2$. Fig. 12(a) and (b) shows the wave propagation behavior in the initial configuration. The value of the objective function J_2 in Eq. (25) is 2.00 with each term $J_{k1} = 1.00$ and $J_{k2} = 1.00$.

We obtained the optimal configuration as a result of optimization, as shown in Fig. 13. Compared with the optimal configuration in Section 5.1, the changes in radius, slope, and aspect ratio of Region $D^{(i)}$ are bigger than the initial configuration. The value of the objective function is 0.0602 with $J_{k1} = 0.0343$ and $J_{k2} = 0.0258$. Fig 12(c) and (d) shows the wave propagation in the optimized system. The value of the first term in the objective function corresponding to the response at $k = k_1$ is 0.0343, and that of the second term corresponding to the response at $k = k_2$ is 0.0258. Fig. 14 shows the homogenized coefficients in the optimal configuration. $a_{11}^{(i)}$ and $a_{22}^{(i)}$ are in the range $4.76 \leq a_{11}^{(i)} \leq 8.27$, $3.17 \leq a_{22}^{(i)} \leq 7.70$ $a_{12}^{(i)}$ and $a_{21}^{(i)}$ are in

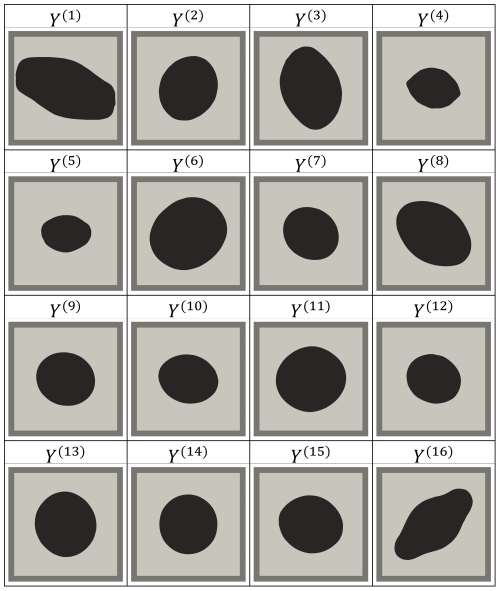

Figure 13: The optimal configrations of unit cells $Y^{(i)}$ obtained in two-frequency optimization.

$-0.602 \leq a_{12}^{(i)} \leq 1.04$, $-0.602 \leq a_{21}^{(i)} \leq 1.04$. At $k = k_1$, Re $\left[\mu^{(i)}\right]$ is negative in $\Omega^{(1)}$, $\Omega^{(3)}$, $\Omega^{(8)}$, $\Omega^{(11)}$, and $\Omega^{(13)}$. At $k = k_2$, μ has a positive real part for all $\Omega^{(i)}$.

Compared with single-frequency optimization, each term of the objective function is larger because the two terms of the objective function are defined at two different frequencies. Fig. 15 shows the frequency response of the terms of the object functions J_{k1} and J_{k2}. They have a peak at $k = 28, 38$, respectively. The wave propagation behavior at $k = k_1$ is similar to that shown in Fig. 9(a) at the point where the bandgap regions with negative permeability contribute to decreasing the objective function. Conversely, there is no bandgap, and the wave propagation behavior is guided only by the distribution of μ at $k = k_2$. The most significant factor is the contrast between $\mu^{(5)}$ and $\mu^{(9)}$, which makes the incident wave travel in the direction of Γ_1 according to the distribution of impedance. The contrast between $\mu^{(4)}$ and $\mu^{(8)}$ behaves similarly. It is interesting to control the waves without using a bandgap caused by the negative real part of $\mu^{(i)}$.

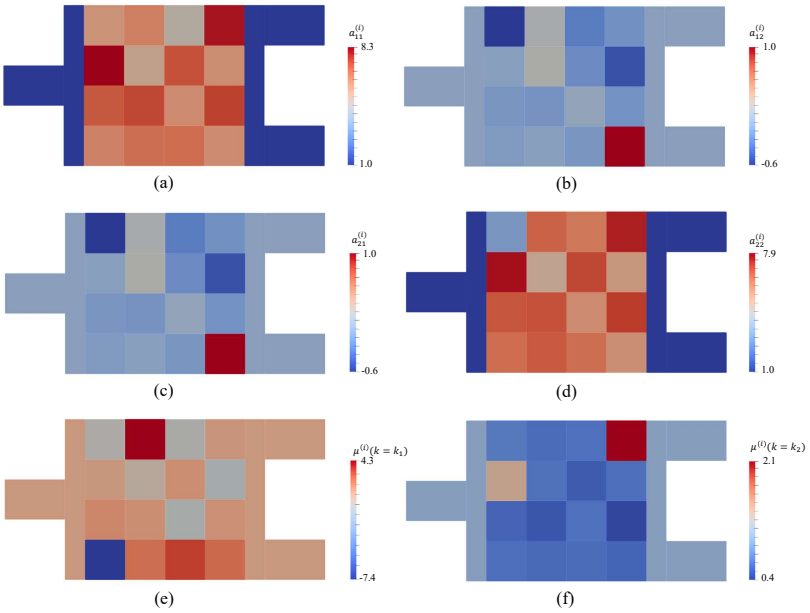

Figure 14: Distribution of the homogenized coefficients. (a): $a_{11}^{(i)}$; (b): $a_{12}^{(i)}$; (c): $a_{21}^{(i)}$; (d): $a_{22}^{(i)}$; (e): Re $\left[\mu^{(i)}\right]$ at $k = k_1$; (f): Re $\left[\mu^{(i)}\right]$ at $k = k_2$.

6. Conclusion

We proposed a multiscale topology optimization method for electromagnetic metamaterials based on the level set-based topology optimization method associated with the high-contrast homogenized method. The results obtained are summarized as follows:

- The high-contrast homogenized method is introduced in the system of electromagnetic metamaterials based on previous studies. A multiscale topology optimization problem is formulated where the objective function is defined with the macroscale wave propagation behavior and the microscale unit cell configuration as design variables.
- The design sensitivities are calculated based on the concepts of topological and shape derivatives.
- Using the proposed method, single-frequency and two-frequency optimization problems were resolved. We obtained the optimal configuration of the unit cells, and the incident waves

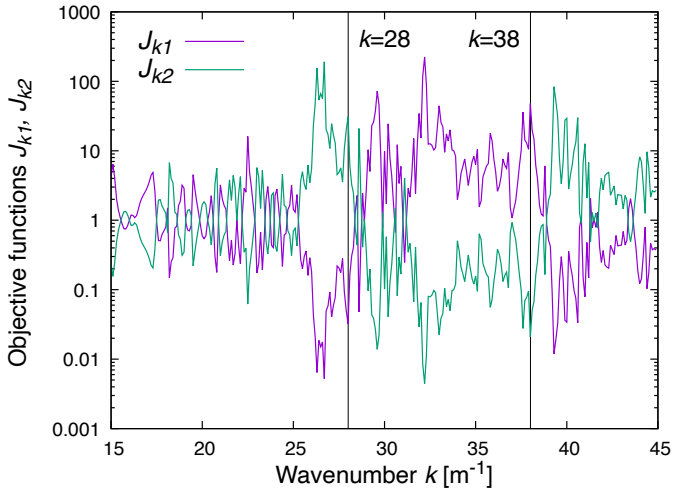

Figure 15: Frequency response of the terms of the objective function J_{k1} and J_{k2}.

were guided to the target boundary corresponding to the frequency. The designed metamaterial control wave propagation behavior using the bandgap caused by the negative real part of permeability and the distribution of wave impedance.

- The optimization results were verified by the Helmholtz equation solved on a system with an array of optimal unit cells.

This method allows for optimal configurations that include metamaterials that operate over a wide frequency band. One of the prospects of this method is its extension to three-dimensional problems that require the introduction of high-contrast homogenization methods in the Maxwell equations. Additionally, the method can be applied to elastic waves and the design of elastic metamaterials.

Acknowledgements

This work was supported in part by JSPS KAKENHI [grant number 20K14636].

Appendix A. Derivation of shape derivative and topological derivative

We explain process of derivation topological derivatives and shape derivatives. First we derive shape derivatives. The Lagrangian L is defined based on Céa's method [33] as follows:

$$\begin{aligned} L(Y^{(i)}, \hat{\boldsymbol{U}}, \hat{\boldsymbol{V}}) = J(u) &+ 2\mathrm{Re}\left[\sum_{i=1}^{N}\int_{\Omega^{(i)}} a_{\mathrm{eff}}^{(i)}\nabla\hat{u}\cdot\nabla\hat{\psi} - k^2\mu_{\mathrm{eff}}^{(i)}\hat{u}\hat{\psi}d\boldsymbol{x} - \int_{\partial G} g\hat{\psi}d\Gamma\right] \\ &+ 2\mathrm{Re}\left[\sum_{i=1}^{N}\sum_{j,k}\hat{\lambda}_{a_{jk}}^{(i)}(a_{jk}^{(i)} - \hat{a}_{jk}^{(i)})\right] + 2\mathrm{Re}\left[\sum_{i=1}^{N}\hat{\lambda}_{\mu}^{(i)}(\mu^{(i)} - \hat{\mu}^{(i)})\right] \\ &- \sum_{i=1}^{N}\int_{Y^{*(i)}} \varepsilon_e^{-1}(\boldsymbol{e}_j + \nabla_y\hat{w}_j^{(i)})\cdot\nabla_y\hat{\psi}_1^{(i)}dy \\ &- 2\mathrm{Re}\left[\sum_{i=1}^{N}\int_{D^{(i)}} \varepsilon_i^{-1}\nabla_y\hat{w}^{(i)}\cdot\nabla_y\hat{\psi}_2^{(i)} - k^2\hat{w}\hat{\psi}_2^{(i)} - \hat{\psi}_2^{(i)}\right]. \end{aligned} \tag{A.1}$$

The variables $\hat{\boldsymbol{U}} = (\hat{u}, \hat{a}_{jk}^{(i)}, \hat{\mu}^{(i)}, \hat{w}_j^{(i)}, \hat{w}^{(i)})$ correspond to state variables, and Lagrange multipliers $\hat{\boldsymbol{V}} = (\hat{\psi}, \hat{\lambda}_{a_{jk}}^{(i)}, \hat{\lambda}_{\mu}^{(i)}, \hat{\psi}_1^{(i)}, \hat{\psi}_2^{(i)})$ correspond to adjoint variables. At the stationary point of L, the optimality conditions are given as

follows:

$$\left\langle \frac{\partial L}{\partial \hat{u}}, \delta\hat{u} \right\rangle \Big|_{\text{opt}} = 0, \tag{A.2}$$

$$\left\langle \frac{\partial L}{\partial \hat{a}_{jk}^{(i)}}, \delta\hat{a}_{jk}^{(i)} \right\rangle \Big|_{\text{opt}} = 0, \tag{A.3}$$

$$\left\langle \frac{\partial L}{\partial \hat{\mu}^{(i)}}, \delta\hat{\mu}^{(i)} \right\rangle \Big|_{\text{opt}} = 0, \tag{A.4}$$

$$\left\langle \frac{\partial L}{\partial \hat{w}_{j}^{(i)}}, \delta\hat{w}_{j}^{(i)} \right\rangle \Big|_{\text{opt}} = 0, \tag{A.5}$$

$$\left\langle \frac{\partial L}{\partial \hat{w}^{(i)}}, \delta\hat{w}^{(i)} \right\rangle \Big|_{\text{opt}} = 0, \tag{A.6}$$

$$\left\langle \frac{\partial L}{\partial \hat{\psi}}, \delta\hat{\psi} \right\rangle \Big|_{\text{opt}} = 0, \tag{A.7}$$

$$\left\langle \frac{\partial L}{\partial \hat{\lambda}_{a_{jk}}^{(i)}}, \delta\hat{\lambda}_{a_{jk}}^{(i)} \right\rangle \Big|_{\text{opt}} = 0, \tag{A.8}$$

$$\left\langle \frac{\partial L}{\partial \hat{\lambda}_{\mu}^{(i)}}, \delta\hat{\lambda}_{\mu}^{(i)} \right\rangle \Big|_{\text{opt}} = 0, \tag{A.9}$$

$$\left\langle \frac{\partial L}{\partial \hat{\psi}_{1}^{(i)}}, \delta\hat{\psi}_{1}^{(i)} \right\rangle \Big|_{\text{opt}} = 0, \tag{A.10}$$

$$\left\langle \frac{\partial L}{\partial \hat{\psi}_{2}^{(i)}}, \delta\hat{\psi}_{2}^{(i)} \right\rangle \Big|_{\text{opt}} = 0. \tag{A.11}$$

The expression in brackets is the directional derivative of the function, and opt represents the stationary point. If the conditions (A.7)–(A.11) are met, $\hat{u} = u$, $\hat{a}_{jk}^{(i)} = a_{jk}^{(i)} =$, $\hat{\mu}^{(i)} = \mu^{(i)}$, $\hat{w}_{j}^{(i)} = w_{j}^{(i)}$ and $\hat{w}^{(i)} = w^{(i)}$ hold at the stationary point.

To satisfy the optimal condition (A.2), an adjoint equation is given as

follows:

$$\sum_{i=1}^{N}\left[\int_{\Omega^{(i)}} a_{\text{eff}}^{(i)}\nabla v_1\cdot\nabla\psi - k^2\mu_{\text{eff}}^{(i)}v_1\psi d\boldsymbol{y}\right] - ik\int_{\Gamma_{\text{in}},\Gamma_1,\Gamma_2} v_1\psi d\Gamma$$
$$+\frac{1}{W_2}\int_{\Gamma_1} u^*\psi d\Gamma - \frac{W_1}{W_2^2}\int_{\Gamma_2} u^*\psi d\Gamma = 0, \tag{A.12}$$
$$\sum_{i=1}^{N}\left[\int_{\Omega^{(i)}} a_{\text{eff}}^{(i)}\nabla v_2\cdot\nabla\psi - k^2\mu_{\text{eff}}^{(i)}v_2\psi d\boldsymbol{y}\right] - ik\int_{\Gamma_{\text{in}},\Gamma_1,\Gamma_2} v_2\psi d\Gamma$$
$$-\frac{W_2}{W_1^2}\int_{\Gamma_1} u^*\psi d\Gamma + \frac{1}{W_1}\int_{\Gamma_2} u^*\psi d\Gamma = 0. \tag{A.13}$$

Here, $W_1 = \int_{\Gamma_1}|u|^2 d\Gamma, W_2 = \int_{\Gamma_2}|u|^2 d\Gamma$, and u^* is complex conjugate of u. v_1 and v_2 are adjoint variables corresponding to objective functions J_{k1} and J_{k2}, and ψ is a test function. The optimal conditions (A.3), (A.4) are expressed as follows:

$$\left\langle \frac{\partial L}{\partial \hat{a}_{jk}^{(i)}}, \delta\hat{a}_{jk}^{(i)}\right\rangle = 2\text{Re}\left[\int_{\Omega^{(i)}}\delta\hat{a}_{jk}^{(i)}\nabla u\cdot\nabla\psi d\boldsymbol{x}\right] - 2\text{Re}\left[\sum_{j,k}\lambda_{a_{jk}}^{(i)}\delta\hat{a}_{jk}^{(i)}\right] \tag{A.14}$$
$$= 0, \tag{A.15}$$
$$\left\langle \frac{\partial L}{\partial \hat{\mu}^{(i)}}, \delta\hat{\mu}^{(i)}\right\rangle = -2\text{Re}\left[\int_{\Omega^{(i)}} k^2\delta\hat{\mu}^{(i)}u\psi d\boldsymbol{x}\right] - 2\text{Re}\left[\lambda_{\mu}^{(i)}\delta\hat{\mu}^{(i)}\right] \tag{A.16}$$
$$= 0. \tag{A.17}$$

Hence, the optimal Lagrange multipliers $\lambda_{a_{jk}}^{(i)}$ and $\lambda_{\mu}^{(i)}$ are given as follows:

$$\lambda_{a_{jk}}^{(i)} = \int_{\Omega^{(i)}}\frac{\partial u}{\partial x_k}\frac{\partial\psi}{\partial x_j}d\boldsymbol{x}, \tag{A.18}$$
$$\lambda_{\mu}^{(i)} = -\int_{\Omega^{(i)}} k^2 u\psi d\boldsymbol{x}. \tag{A.19}$$

Similarly, the optimal conditions (A.5) and (A.6) are expressed as follows:

$$\begin{aligned}\left\langle \frac{\partial L}{\partial \hat{w}_j^{(i)}}, \delta\hat{w}_j^{(i)} \right\rangle =& 2\mathrm{Re}\left[\lambda_{a_{jk}}^{(i)}\right]\left\{\int_{\partial Y^{*(i)}} \boldsymbol{n}\cdot(\varepsilon_e^{-1}\boldsymbol{e}_k)\delta\hat{w}_j^{(i)}d\Gamma - \int_{Y^{*(i)}} \nabla_y\cdot(\varepsilon_e^{-1}\boldsymbol{e}_k)\delta\hat{w}_j^{(i)}d\Gamma\right\}\\ &- \int_{\partial Y^{*(i)}} \boldsymbol{n}\cdot(\varepsilon_e^{-1}\nabla_y\delta\hat{w}_j^{(i)})(\psi_1^{(i)}+\mu)d\Gamma - \int_{Y^{*(i)}} \nabla_y\cdot(\varepsilon_e^{-1}\nabla_y\psi_1^{(i)})\delta w_j^{(i)}d\boldsymbol{y}\\ &+ \int_{\partial Y^{*(i)}} \boldsymbol{n}\cdot(\varepsilon_e^{-1}\nabla_y\psi_1^{(i)})\delta\hat{w}_j^{(i)}d\Gamma\\ =&0, \end{aligned} \tag{A.20}$$

$$\begin{aligned}\left\langle \frac{\partial L}{\partial \hat{w}^{(i)}}, \delta\hat{w}^{(i)} \right\rangle =& 2\mathrm{Re}\left[\lambda_\mu^{(i)}\int_{D^{(i)}} k^2\delta\hat{w}^{(i)}d\Gamma\right]\\ &-2\mathrm{Re}\left[\int_{\partial Y^{*(i)}} \boldsymbol{n}\cdot(\varepsilon_i^{-1}\nabla_y\delta\hat{w}^{(i)})pd\Gamma\right]\\ &-2\mathrm{Re}\left[\int_{D^{(i)}}\left\{\varepsilon_i^{-1}\nabla_y\psi_2^{(i)}\cdot\nabla_y\delta\hat{w}^{(i)} - k^2\psi_2^{(i)}\delta\hat{w}^{(i)}\right\}d\boldsymbol{y}\right]\\ &+2\mathrm{Re}\left[\int_{\partial D^{(i)}}\delta\hat{w}^{(i)}\hat{\mu}d\Gamma\right]\\ =&0. \end{aligned} \tag{A.21}$$

Therefore, the optimal Lagrange multipliers $\psi_1^{(i)}$ and $\psi_2^{(i)}$ are given as follows:

$$\psi_1^{(i)} = 2\mathrm{Re}\left[\lambda_{a_{jk}}^{(i)}\right]w_k^{(i)}, \tag{A.22}$$

$$\psi_2^{(i)} = -\lambda_\mu^{(i)}k^2w^{(i)}. \tag{A.23}$$

Shape derivative is derived using the following relationship between functional and shape derivative shown by a previous study [39]:

$$J(\Omega) = \int_\Omega f(\boldsymbol{y})d\Omega \quad\rightarrow\quad DJ\cdot\boldsymbol{\theta} = \int_{\partial\Omega}\boldsymbol{\theta}(\boldsymbol{y})\cdot\boldsymbol{n}(\boldsymbol{y})f(\boldsymbol{y})d\Gamma, \tag{A.24}$$

$$J(\Omega) = \int_{\partial\Omega} f(\boldsymbol{y})d\Gamma \quad\rightarrow\quad DJ\cdot\boldsymbol{\theta} = \int_{\partial\Omega}\boldsymbol{\theta}\cdot\boldsymbol{n}(\frac{\partial f}{\partial n} + Hf)d\Gamma. \tag{A.25}$$

Shape derivative is derived using Eqs. (A.24) and (A.25) corresponding to each objective function. H is the mean curvature on $\partial\Omega$ given as $H = \mathrm{div}\boldsymbol{n}$. Using this relationship, the shape derivatives of the objective functions in Eqs. (26) and (27) are derived as in Eqs. (34) and (37), respectively.

Next, we derive toplogical derivative from shape derivatives. Novotny et al. [34] and Feijóo et al. [35] showed that topological derivative is given by the limit value of shape drivatives as follows:

$$D_T J = \lim_{\varepsilon \to 0} \frac{DJ \cdot \boldsymbol{\theta}}{V'(\varepsilon)|\theta_n|}. \tag{A.26}$$

$V'(\varepsilon)$ is derivative of $V(\varepsilon)$ for ε. This relationship holds for shape derivatives assuming shape changes where the circular Region Ω_ε expands using the negative constant θ_n and the outward unit normal vector $\boldsymbol{n}$ in the Region Ω_0. This is expressed as $\boldsymbol{\theta} = \theta_n \boldsymbol{n}$. Since $w_j^{(i)}$ depends on the radius ε in the shape change, we denote $w_j^{(i)}$ as $w_j^{(i)\varepsilon}$. The shape derivative is rewritten as follows:

$$\begin{aligned} &DJ(Y^{(i)}) \cdot \boldsymbol{\theta} \\ =&2\mathrm{Re}\left[\lambda_{a_{jk}}^{(i)}\right] \int_{\partial Y^{*(i)}} (\boldsymbol{\theta} \cdot \boldsymbol{n}) \varepsilon_e^{-1} \left(\delta_{jk} + \frac{\partial w_j^{(i)\varepsilon}}{\partial y_k} + \frac{\partial w_k^{(i)\varepsilon}}{\partial y_j} + \nabla_y w_j^{(i)\varepsilon} \cdot \nabla_y w_k^{(i)\varepsilon} \right) d\Gamma. \end{aligned} \tag{A.27}$$

When $\varepsilon \to 0$, $w_j^{(i)\varepsilon}$ exhibits the following asymptotic behavior, as shown in previous study [29].

$$\begin{cases} w_j^{(i)\varepsilon} \to w_j^{(i)0}(\boldsymbol{y}_0), \\ \nabla_y w_j^{(i)\varepsilon} \to \nabla_y w_j^{(i)0}|_{\boldsymbol{y}_0} + \nabla_\xi H(\boldsymbol{\xi}). \end{cases} \tag{A.28}$$

$w_j^{(i)0}$ denotes $w_j^{(i)}$ before Ω_ε is introduced. $\boldsymbol{y}_0$ is the point at the center of Ω_ε and $\boldsymbol{\xi} = (\boldsymbol{y} - \boldsymbol{y_0})/\varepsilon$ denotes the coordinates of $\boldsymbol{y}$ normalized by the radius ε. $H(\boldsymbol{\xi})$ is given as follows in polar coordinate (r, θ) of $\boldsymbol{\xi}$ [29]:

$$H(r,\theta) = \frac{1}{r} \left\{ \left(\left. \frac{\partial w_j^{(i)0}}{\partial y_1} \right|_{\boldsymbol{y}_0} + \delta_{j1} \right) \cos\theta + \left(\left. \frac{\partial w_j^{(i)0}}{\partial y_2} \right|_{\boldsymbol{y}_0} + \delta_{j2} \right) \sin\theta \right\} \tag{A.29}$$

Using Eq. (A.28), the limit of shape delivative (A.27) to $\varepsilon \to 0$ is expressed as follows:

$$\begin{aligned} &DJ(Y^{(i)}) \cdot \boldsymbol{\theta} \\ &\xrightarrow[\varepsilon \to 0]{} 4\pi\varepsilon\theta_n \mathrm{Re}\left[\lambda_{a_{jk}}^{(i)}\right] \varepsilon_e^{-1} \{ \delta_{jk} + \boldsymbol{e}_j \cdot \nabla_y w_k^0|_{\boldsymbol{y}_0} + \boldsymbol{e}_k \nabla_y w_j^0|_{\boldsymbol{y}_0} \\ &+ 2\nabla_y w_j^0|_{\boldsymbol{y}_0} \cdot \nabla_y w_k^0|_{\boldsymbol{y}_0} \delta_{kl} \frac{\partial w_j^0}{\partial y_l}|_{\boldsymbol{y}_0} + \delta_{jl} \frac{\partial w_k^0}{\partial y_l}|_{\boldsymbol{y}_0} + \delta_{jl}\delta_{kl} \}. \end{aligned} \tag{A.30}$$

Using the above limits and Eq. (A.26), the topological derivative can be derived as in Eq. (42).

Competing interests

The authors declare no conflicts of interest.

Author contributions statement

The authors confirm contribution to the paper as follows: Naoki Murai: Conceptualization, Methodology, Software, Validation, Formal analysis, Investigation, Data Curation, Writing-Original Draft, Visualization. Yuki Noguchi: Conceptualization, Methodology, Software, Formal analysis, Data curation, Writing-Review & Editing, Funding acquisition. Kei Matsushima: Methodology, Software, Writing-Review & Editing. Takayuki Yamada: Methodology, Software, Resources, Data curation, Writing-Review & Editing, Project administration, Supervision.

References

[1] J. B. Pendry, A. J. Holden, D. J. Robbins, W. Stewart, Magnetism from conductors and enhanced nonlinear phenomena, IEEE transactions on microwave theory and techniques 47 (11) (1999) 2075–2084.

[2] D. R. Smith, W. J. Padilla, D. Vier, S. C. Nemat-Nasser, S. Schultz, Composite medium with simultaneously negative permeability and permittivity, Physical review letters 84 (18) (2000) 4184.

[3] G. Bouchitté, D. Felbacq, Homogenization near resonances and artificial magnetism from dielectrics, Comptes Rendus Mathematique 339 (5) (2004) 377–382.

[4] V. G. Veselago, The electrodynamics of substances with simultaneously negative values of ϵ and μ, Physics-Uspekhi 10 (4) (1968) 509–514.

[5] S. Haxha, F. AbdelMalek, F. Ouerghi, M. Charlton, A. Aggoun, X. Fang, Metamaterial superlenses operating at visible wavelength for imaging applications, Scientific Reports 8 (1) (2018) 1–15.

[6] M. Jung, N. Heo, J. Park, J. Yoo, Multi-directional cloaking structure design using topology optimization, Journal of Electromagnetic Waves and Applications 35 (8) (2021) 1008–1019.

[7] A. T. Devapriya, S. Robinson, Investigation on metamaterial antenna for terahertz applications, Journal of Microwaves, Optoelectronics and Electromagnetic Applications 18 (2019) 377–389.

[8] M. Noda, Y. Noguchi, T. Yamada, Extended level set method: A multiphase representation with perfect symmetric property, and its application to multi-material topology optimization, Computer Methods in Applied Mechanics and Engineering 393 (2022) 114742.

[9] T. Yamada, Y. Noguchi, Topology optimization with a closed cavity exclusion constraint for additive manufacturing based on the fictitious physical model approach, Additive Manufacturing 52 (2022) 102630. doi:https://doi.org/10.1016/j.addma.2022.102630.
URL https://www.sciencedirect.com/science/article/pii/S2214860422000379

[10] M. P. Bendsøe, N. Kikuchi, Generating optimal topologies in structural design using a homogenization method, Computer methods in applied mechanics and engineering 71 (2) (1988) 197–224.

[11] T. Yamada, K. Izui, S. Nishiwaki, A level set-based topology optimization method for maximizing thermal diffusivity in problems including design-dependent effects (2011).

[12] L. Alacoque, R. T. Watkins, A. Y. Tamijani, Stress-based and robust topology optimization for thermoelastic multi-material periodic microstructures, Computer Methods in Applied Mechanics and Engineering 379 (2021) 113749. doi:https://doi.org/10.1016/j.cma.2021.113749.
URL https://www.sciencedirect.com/science/article/pii/S0045782521000852

[13] Y. Noguchi, T. Yamada, Topology optimization for acoustic structures considering viscous and thermal boundary layers using a sequential linearized navier–stokes model, Computer Methods in Applied Mechanics and Engineering 394 (2022) 114863.

[14] R. E. Christiansen, O. Sigmund, Inverse design in photonics by topology optimization: tutorial, JOSA B 38 (2) (2021) 496–509.

[15] A. R. Diaz, O. Sigmund, A topology optimization method for design of negative permeability metamaterials, Structural and Multidisciplinary Optimization 41 (2) (2010) 163–177.

[16] M. Otomori, T. Yamada, K. Izui, S. Nishiwaki, J. Andkjær, A topology optimization method based on the level set method for the design of negative permeability dielectric metamaterials, Computer Methods in Applied Mechanics and Engineering 237 (2012) 192–211.

[17] R. E. Christiansen, O. Sigmund, Designing meta material slabs exhibiting negative refraction using topology optimization, Structural and Multidisciplinary Optimization 54 (3) (2016) 469–482.

[18] D. Smith, D. Vier, T. Koschny, C. Soukoulis, Electromagnetic parameter retrieval from inhomogeneous metamaterials, Physical review E 71 (3) (2005) 036617.

[19] S. Arslanagić, T. V. Hansen, N. A. Mortensen, A. H. Gregersen, O. Sigmund, R. W. Ziolkowski, O. Breinbjerg, A review of the scattering-parameter extraction method with clarification of ambiguity issues in relation to metamaterial homogenization, IEEE Antennas and Propagation Magazine 55 (2) (2013) 91–106.

[20] E. Sánchez-Palencia, Non-homogeneous media and vibration theory, Lecture notes in physics 127 (1980).

[21] N. S. Bakhvalov, G. Panasenko, Homogenisation: averaging processes in periodic media: mathematical problems in the mechanics of composite materials, Vol. 36, Springer Science & Business Media, 2012.

[22] A. Bensoussan, J.-L. Lions, G. Papanicolaou, Asymptotic analysis for periodic structures, Vol. 374, American Mathematical Soc., 2011.

[23] V. P. Smyshlyaev, K. D. Cherednichenko, On rigorous derivation of strain gradient effects in the overall behaviour of periodic heterogeneous media, Journal of the Mechanics and Physics of Solids 48 (6-7) (2000) 1325–1357.

[24] A. Abdulle, M. J. Grote, C. Stohrer, Finite element heterogeneous multiscale method for the wave equation: long-time effects, Multiscale Modeling & Simulation 12 (3) (2014) 1230–1257.

[25] T. Dohnal, A. Lamacz, B. Schweizer, Bloch-wave homogenization on large time scales and dispersive effective wave equations, Multiscale Modeling & Simulation 12 (2) (2014) 488–513.

[26] R. V. Craster, J. Kaplunov, A. V. Pichugin, High-frequency homogenization for periodic media, Proceedings of the Royal Society A: Mathematical, Physical and Engineering Sciences 466 (2120) (2010) 2341–2362.

[27] M. Ohlberger, B. Verfurth, A new heterogeneous multiscale method for the helmholtz equation with high contrast, Multiscale Modeling & Simulation 16 (1) (2018) 385–411.

[28] G. Zhang, K. Khandelwal, Computational design of finite strain auxetic metamaterials via topology optimization and nonlinear homogenization, Computer Methods in Applied Mechanics and Engineering 356 (2019) 490–527.

[29] Y. Noguchi, T. Yamada, Topology optimization of acoustic metasurfaces by using a two-scale homogenization method, Applied Mathematical Modelling 98 (2021) 465–497.

[30] T. Yamada, K. Izui, S. Nishiwaki, A. Takezawa, A topology optimization method based on the level set method incorporating a fictitious interface energy, Computer Methods in Applied Mechanics and Engineering 199 (45-48) (2010) 2876–2891.

[31] G. Allaire, Homogenization and two-scale convergence, SIAM Journal on Mathematical Analysis 23 (6) (1992) 1482–1518.

[32] F. Feppon, G. Michailidis, M. Sidebottom, G. Allaire, B. Krick, N. Vermaak, Introducing a level-set based shape and topology optimization method for the wear of composite materials with geometric constraints, Structural and Multidisciplinary Optimization 55 (2) (2017) 547–568.

[33] J. Cea, Conception optimale ou identification de formes, calcul rapide de la dérivée directionnelle de la fonction coût, ESAIM: Mathematical Modelling and Numerical Analysis - Modélisation Mathématique et

Analyse Numérique 20 (3) (1986) 371–402.
URL http://www.numdam.org/item/M2AN_1986__20_3_371_0/

[34] A. A. Novotny, R. A. Feijóo, E. Taroco, C. Padra, Topological sensitivity analysis, Computer methods in applied mechanics and engineering 192 (7-8) (2003) 803–829.

[35] R. A. Feijóo, A. A. Novotny, E. Taroco, C. Padra, The topological derivative for the poisson's problem, Mathematical models and methods in applied sciences 13 (12) (2003) 1825–1844.

[36] F. Hecht, New development in freefem++, J. Numer. Math. 20 (3-4) (2012) 251–265.
URL https://freefem.org/

[37] C. Dapogny, C. Dobrzynski, P. Frey, Three-dimensional adaptive domain remeshing, implicit domain meshing, and applications to free and moving boundary problems, Journal of computational physics 262 (2014) 358–378.

[38] G. Michailidis, Manufacturing constraints and multi-phase shape and topology optimization via a level-set method, Ph.D. thesis, Ecole Polytechnique X (2014).

[39] G. Allaire, F. Jouve, A.-M. Toader, Structural optimization using sensitivity analysis and a level-set method, Journal of computational physics 194 (1) (2004) 363–393.